Published in final edited form as:

Nat Chem Biol. 2019 December ; 15(12): 1183–1190. doi:10.1038/s41589-019-0405-4.

Optogenetic control of Cofilin and αTAT in living cells using Z-lock

Orrin J. Stone[1,†], **Neha Pankow**[1,†], **Bei Liu**[1,†], **Ved P. Sharma**[3,4], **Robert J. Eddy**[3], **Hui Wang**[1], **Andrew T. Putz**[1], **Frank D Teets**[6], **Brian Kuhlman**[6], **John S. Condeelis**[3,4,5,*], **Klaus M. Hahn**[1,2,*]

[1]Department of Pharmacology, University of North Carolina, Chapel Hill, NC, USA.

[2]Lineberger Cancer Center, University of North Carolina at Chapel Hill, Chapel Hill, North Carolina, USA.

[3]Department of Anatomy and Structural Biology, Albert Einstein College of Medicine, New York, NY, USA.

[4]Gruss Lipper Biophotonics Center, Albert Einstein College of Medicine, New York, NY, USA.

[5]Integrated Imaging Program, Albert Einstein College of Medicine, New York, NY, USA.

[6]Department of Biochemistry and Biophysics, University of North Carolina, Chapel Hill, NC, USA

Abstract

Here we introduce Z-lock, an optogenetic approach for reversible, light-controlled steric inhibition of protein active sites. The LOV domain and Zdk, a small protein that binds LOV selectively in the dark, are appended to the protein of interest where they sterically block the active site. Irradiation causes LOV to change conformation and release Zdk, exposing the active site. Computer-assisted protein design was used to optimize linkers and Zdk-LOV affinity, for both effective binding in the dark, and effective light-induced release of the intramolecular interaction. Z-lock cofilin was shown to have actin severing ability in vitro, and in living cancer cells it produced protrusions and invadopodia. An active fragment of the tubulin acetylase αTAT was similarly modified and shown to acetylate tubulin upon irradiation.

Introduction

The cofilin pathway has been implicated in tumor cell migration during the early stages of metastasis. [1] Rapid cofilin activation in specific cellular compartments results in the severing of actin filaments. [2–4] Local F-actin severing by cofilin can produce either polymerization or

*Correspondence: John.condeelis@einstein.yu.edu, khahn@med.unc.edu.
†Equal contribution

Author Contributions: J.C. and K.M.H. conceived of the project. O.S., B.L. and N.P. carried out the experiments, with assistance and advice from V.S. and R.J.E. in live cell imaging and assay of effects on cofilin. K.H. and H.W. conceived of Z-lock, and J.S.C. initiated the focus on cofilin. K.M.H. and J.S.C. supervised the project. O.S., F. T. and B. K. performed Rosetta modeling. A.P. purified proteins. O.S. and K.M.H. wrote the manuscript with input from all authors.

Competing Financial Interests Statement: The authors declare no competing financial interests.

depolymerization of F-actin depending on the location and timing of cofilin activation. [1,5,6] Conventional approaches to understand the role of cofilin in cell motility have not been sufficient to decipher important mechanistic questions; cofilin overexpression or suppression are complicated by cellular compensation, lack of kinetic information and a lack of spatial control, which impedes detection of the immediate effects of cofilin activation. [7–9] To address these concerns, we sought an optogenetic analog of cofilin that could be activated locally with precise kinetics.

We previously produced a photo-activatable cofilin analog by attaching a photocleavable protecting group to a constitutively active cofilin mutant. [10] Irradiation of this analog produced cofilin-dependent localized actin polymerization in living cells, but activation was irreversible and led to accumulation of active cofilin. Furthermore, production of the analog required cofilin isolation, chemical labeling and reinjection. Recently, a genetically-encoded photoactivatable cofilin based on the Lifeact peptide was produced. [11,12] However, a subsequent study demonstrated that Lifeact significantly alters cofilin severing activity, which prevented us from using the probe to study cofilin-mediated F-actin severing during tumor cell migration. [13]

Due to these issues we developed Z-lock, a new optogenetic approach with potentially broad utility, and applied it to cofilin. To demonstrate the versatility of the method, we also generated a light controlled analog of the alpha tubulin acetylase αTAT. Z-lock was based on the LOV2 domain of *Avena Sativa* phototropin 1, a protein of proven utility for optogenetics, and the basis of several optogenetics approaches. [14–21] The C terminal helix of LOV2 unwinds reversibly in response to irradiation between 400–500 nm. Unwinding is rapid (< 0.5 milliseconds) and the rate of return to the folded state is tunable, with point mutations producing t1/2 of 1.7 – 496 seconds. [22–24] Z-lock also made use of Zdk, a protein A fragment we developed previously that binds selectively to the dark conformation of LOV2. [24,25] As shown in Figure 1a, Zdk and LOV2 were attached to the C- and N-termini of cofilin such that they bound to each other in the dark and formed a loop occluding the active site. Upon irradiation, Zdk and LOV unlinked, freeing the active site. Because photocontrol was based upon steric inhibition, Z-lock could potentially be applied to diverse proteins or protein fragments with specific activity. The most important requirement was appropriate orientation of the two termini, which we achieved with linker optimization, and which could in some cases benefit from circular permutation. [26]

We previously used Zdk in another optogenetic approach, named LOVTRAP[24], to sequester molecules at particular subcellular locations. LOVTRAP relied on the binding of Zdk to LOV in the dark, which held the target protein on organelles such as mitochondria until it was released by irradiation. Here we use LOV and Zdk to build an intramolecular bridge over the target proteins' active sites. Building this bridge presented challenges in protein engineering different from those encountered with LOVTRAP. We had to adjust the affinity of the binding components to accommodate the intramolecular interaction of Zdk and LOV, and had to properly orient the bridge they formed upon binding. Z-lock produced an active protein that could be turned on and off wherever it was, not a protein that was sequestered and reversibly released. The fluorescent protein DRONPA has also been used to control proteins through light-regulated homodimerization over their active site[27,28]. Z-lock's most

important advantages are the ability to adjust the affinity and kinetics of the Zdk-LOV interaction, and the relatively small size of LOV and Zdk, facilitating engineering.

This paper describes the engineering and placement of a light-modulated bridge over the active sites of both cofilin and αTAT. We make use of a linker, built into the middle of the bridge, that can be reversibly perturbed by irradiation, and the engineering involved for proper placement and affinity of the linker components. This results in a set of tools that can be valuable for similarly controlling other protein active sites.

Results

Development and optimization of Z-lock cofilin

Cryo-EM structures of cofilin bound to F-actin show that the C-terminus is free and solvent exposed, and previous studies have demonstrated that GFP fused to cofilin's C-terminus does not interfere with cofilin function. [29] However, cofilin's N-terminus makes several contacts with F-actin. Therefore, we tested whether fusion of Zdk to cofilin's N-terminus affected F-actin binding (Supplementary Fig. 1a). For this, we used a well characterized assay that measures the ability of cofilin to co-sediment with actin during ultracentrifugation (Supplementary Fig. 1b, Supplementary Fig. 2). [30] Zdk fusion affected neither F-actin binding nor cofilin's ability to convert F-actin to G-actin (Supplementary Figs. 1c and 1d, Supplementary Figs. 2a–2g and 3a–3d).

To produce light-controlled steric inhibition of cofilin, we needed to position the Zdk-LOV complex where it would block cofilin F-actin binding in the dark state, but not in the lit state. To find appropriate linkers, we performed Rosetta structure prediction simulations and assessed the orientation of the Zdk-LOV complex relative to the active site (Methods). [31] We were able to achieve correct positioning by combining a 5 a.a. N-terminal linker and an 8 a.a. C-terminal linker (Fig. 1b). With longer linkers, the complex failed to reliably orient over cofilin's actin binding site. For linkers that were too short, the Rosetta algorithm was unable to form the LOV-Zdk complex over cofilin, indicating that Zdk and LOV would not reach each other to bind in the dark. We tested two variants of Zdk (Zdk1 and Zdk2), with different affinity and Zdk-LOV binding sites, to see which produced light-dependent F-actin interactions. They were compared using the co-sedimentation assay and LOV2 mutants that mimicked the lit and dark conformations. Zdk1 achieved a modest (≈ 50%) reduction in F-actin binding in the dark state that fully recovered in the lit state (Fig. 2a, GSGGG lane). Zdk2 produced more robust inhibition (≈ 80%) in the dark state, but activity was not recovered in the lit state (Fig. 2b–2c, Supplementary Fig. 4, Cofilin and Zdk2 Cofilin LOV lanes).

We attempted to improve the dark state inhibition of the Zdk1 design. Comparing structural models of the Zdk1 and Zdk2 designs revealed a potentially strained linker conformation connecting Zdk1 to cofilin, which we hypothesized was hindering Zdk1 binding to dark state LOV2 (Fig. 1b). To improve the Zdk1 design, we tested whether removing a proline and/or lysine from the C-terminus of Zdk1 would enhance linker flexibility and improve binding to dark state LOV2. In rapid optimization studies using single tests of multiple different

linkers, one linker was found to produce a 3-fold reduction in dark state binding, but lit state binding was also reduced (Fig. 2a and Supplementary Fig. 5).

We turned to optimizing the Zdk2 design based on the hypothesis that Zdk2 was binding too tightly to LOV2. This was reasonable given robust inhibition in both the lit and dark conformation, the higher affinity of Zdk2 for lit state LOV (Zdk2: 761 ± 78 nM; Zdk1: > 4 μM) [24], and the fact that in our design the two proteins were physically linked together (Fig. 2d). We reasoned that lowering Zdk2 affinity could facilitate dissociation, so we performed Rosetta mutational analysis to identify point mutants that would modestly decrease Zdk2 affinity (Fig. 2e). Mutations were chosen based on two criteria: i) avoiding mutation of residues mediating contact between Zdk2 and the Jα helix of LOV2, as this could reduce selectivity for dark state LOV2, and ii) mutating non-polar residues to other non-polar residues, as this is more accurately modeled by Rosetta. [24,32] To assess each potential mutation, we used Rosetta to calculate the change in Gibbs free energy (ΔΔG) for Zdk2 in isolation and for the Zdk2-LOV2 complex, which yielded the ΔΔG of binding (Fig. 2f). We selected several Zdk2 mutants for testing (V15A, V15I, and I32F) based on their predicted reduction in binding affinity and neutral effect on Zdk2 stability (Supplementary Table 1). All mutants tested displayed increased F-actin binding in the lit state relative to wild type Zdk2 (Fig. 2g and Supplementary Fig. 6). One mutant, Zdk2 I32F, exhibited a roughly five-fold difference in F-actin binding for the lit versus dark state. This analog was selected for further development and was named Z-lock cofilin (Fig. 2b–2c, Supplementary Fig. 4, Z-lock cofilin (I32F) lane, Supplementary Table 2). Co-sedimentation assays showed that the affinity of Z-lock cofilin for actin was 285±44 μM in the dark and 4.5±2.4 μM in the light (Supplementary Fig. 7a – 7b). Rosetta modeling indicated that actin binding was inhibited in the dark state of Z-lock cofilin (Supplementary Figure 8a–8b).

Z-lock cofilin effects on Actin *in vitro* and in cells

To test light-dependent severing of actin by Z-lock Cofilin, we deposited in-vitro polymerized F-actin on coverslips and added lysate from MTLn3 cells expressing Z-lock cofilin. Irradiation of these coverslips led to F-actin severing (Supplementary Fig. 9a–9c), while lysates containing Z-lock cofilin dark state mutant (Supplementary Table 2) had no effect (Supplementary Fig. 9a–9c). To confirm that the F-actin severing was caused by cofilin, we purified wt cofilin and Z-lock cofilin mutants that mimic the lit and dark conformations (Methods, Supplementary Table 2). Wt cofilin and the lit state mutant severed F-actin efficiently, but the dark state mutant did not (Supplementary Fig. 9d). Consistent with previous studies of cofilin[33], Z-lock cofilin in living cells was sequestered in the cytosol until irradiation, when it translocated to the cell edge and co-localized with actin. When irradiation ceased, the Z-lock cofilin returned to its initial distribution (Supplementary Fig. 10).

Previous studies have shown that cofilin promotes tumor cell migration and directionality by initiating actin polymerization at the cell edge. [3,10] We assessed changes in cell migration and F-actin levels following photoactivation of cofilin in live tumor cells. Z-lock cofilin or a dark state mutant control were expressed in the MTLn3 breast cancer cell line, and the effects of cofilin photoactivation were assessed using time lapse fluorescence microscopy. [34]

Analysis of cell perimeters before and after photoactivation revealed localized protrusion at the site of photoactivation for Z-lock cofilin but not for the Z-lock cofilin dark state mutant (Fig. 3a, Movie 1, Supplementary Table 2). We assessed the directionality of cell movement before and after photoactivation by measuring the cosine of the angle between the site of photoactivation and the vector indicating the overall direction of cell movement (Fig. 3b). Photoactivation resulted in reorientation of the vector towards the spot of photoactivation, and a consequent increase in cosine values. No change in cosine values was observed for the dark state mutant control. We next investigated the effect of global photoactivation on F-actin levels in MTLn3 cells (Fig. 3c). The low expression levels of Z-lock cofilin minimally impacted F-actin levels prior to irradiation (Supplementary Fig. 11 a–d). Photoactivation resulted in a significant increase in F-actin at 3 minutes post-activation, closely paralleling the timing and level of F-actin increase induced by epidermal growth factor (EGF) stimulation. [35] This suggested that cofilin-dependent actin severing and free barbed end formation is sufficient to induce increases in F-actin following EGF stimulation. Irradiation of the cell edge produced protrusions that retracted when the light was turned off, indicating that effects were reversible (Fig. 3d). During light-induced protrusion, cells retracted at positions away from the site of irradiation (Fig. 3d). Control cells expressing the dark state mutant of Z-lock cofilin showed no response to light (Fig. 3e). Sequential photoactivation at the cell edge sometimes induced protrusions multiple times, but this was inconsistent (Supplementary Fig. 12a – 12d, Movie 2).

Z-lock induces invadopodia

Metastasis requires dissemination of primary tumor cells to distant organs, where they form secondary tumors. A key step in this process is tumor cell invasion into blood vessels, which is enabled by matrix-degrading protrusions termed ‘invadopodia’. [36] Previous studies indicate that this process is dependent on cofilin; cofilin depletion by RNAi inhibits invadopodium precursor stabilization and results in the slow accumulation of actin cytoskeletal defects that directly affect precursor stabilization and maturation. [1,37] Transient cofilin activation, such as that observed following EGF stimulation, directly contributes to invadopodia precursor stabilization and maturation by driving localized actin polymerization. We therefore assessed the effect of cofilin photoactivation on invadopodium precursor assembly (Fig. 3f). MTLn3 cells expressing either Z-lock cofilin or the Z-lock cofilin dark state mutant were globally irradiated for one minute to mimic the kinetics of cofilin activation following EGF stimulation. The number of invadopodium precursors at different time points was measured by quantifying the number of cortactin- and Tks5-positive puncta, made visible by immunostaining (Fig. 3g). [38] Photoactivation led to a significant increase in invadopodium precursors five minutes after photoactivation (Fig. 3h, 3i). No significant change was observed for the Z-lock cofilin dark state mutant control at any time point. Notably, our results closely match previous findings that precursor formation peaks at five minutes following EGF stimulation. [39]

Z-lock αTAT

To probe the generality of the Z-lock approach, we used it to control a second target, the alpha-tubulin acetyl transferase (αTAT). The level of tubulin acetylation is regulated by the antagonistic actions of αTAT and the tubulin deacetylases, histone deacetylase 6 (HDAC6)

[40,41] and sirtuin type 2 (SIRT2) [42]. SIRT2 has been studied extensively and is known to deacetylate substrates other than tubulin, including the HAT domain of p300 histone acetyl transferase and a histone H4 pepetide[43,44]. αTAT, on the other hand, is highly specific for microtubules and preferentially acetylates microtubules over free tubulin[45]. The functional consequences of alpha tubulin acetylation have been investigated primarily through over-expression or knockdown of the deacetylase or the acetyl transferase. We sought to help define the role of this dynamic modification by producing a tool that can generate acetylation in living cells.

αTAT catalyzes the transfer of an acetyl moiety from acetyl co-A to tubulin. Full length αTAT consists of a catalytic core, a C-terminal extension, and a tail domain[46]. We used the functional core domain (amino acid, a.a. 2 to 236), for which structural information is available[47]. The flexible, unstructured tail was excluded because it contains multiple phosphorylation sites that could affect activity independent of the Z-lock steric block. The N and C- termini of αTAT core are on opposite sides of both the tubulin and acetyl coA binding sites. Blocking either site could effectively inhibit αTAT activity. Fusing the LOV domain alone to the N-terminus of αTAT did not effectively block tubulin-binding.

To engineer a Z-lock analog of αTAT, we fused Zdk1 to the N-terminus of the αTAT core, and LOV2 to the C-terminus (Figure 4a). Western blotting showed that acetylation levels in cells were elevated about two-fold when expressing αTAT core relative to a dominant negative, kinase-dead mutant αTAT (DN αTAT) (Figure 4b–4c, Supplementary Fig. 13, Supplementary Table 2). Using a fixed 10 a.a. (5GS) linker between Zdk1 and αTAT, we tested three different linkers between αTAT and LOV2 (Supplementary Table 2, 4, 6 and 8 a.a., all GS repeats). We found that caging was optimal using the 6 a.a. (3GS) linker. Longer linkers between αTAT and LOV2 could fully recover αTAT activity, but were not as effective at reducing activity in the dark state. Further reduction of linker length resulted in lower light-induced activity. (Figure 4b–4c, Supplementary Table 2) Varying the linker between Zdk1 and αTAT had little effect. The 3GS version was named Z-lock αTAT, and was used in all subsequent experiments.

An initial examination of the αTAT structure indicated three potential inhibition mechanisms. The Z-lock components could sterically occlude the binding site for tubulin or for acetyl CoA, or the binding of Zdk to LOV could distort the αTAT structure without occluding these sites. To examine which of these three mechanisms is most relevant to our designed switch, we performed structure prediction simulations with Rosetta[48,49]. The starting models for the simulations were Zdk fused to the N-terminus of αTAT with the linker (Zdk-GSGSGSGSGS-αTAT) between the two domains in a random conformation and the LOV domain (in the dark state) fused to the C-terminus of αTAT with the linker (αTAT-GSGS-LOV) also in a random conformation. Monte Carlo optimization of the backbone torsion angles in the two linkers was then used to search for low energy models in which Zdk was appropriately docked against the LOV domain. Distance constraints derived from the crystal structure of Zdk bound to the LOV domain were used to direct the docking between Zdk and the LOV domain[24]. 20,000 independent simulations were performed and the models output from each simulation were examined to identify what surfaces of αTAT are occluded when Zdk binds to the LOV domain. In more than 90% of the models the

Zdk/LOV complex is adjacent to the tubulin binding on αTAT and is predicted to sterically occlude binding to tubulin, while the Zdk/LOV complex never came within 6 angstroms of the acetyl CoA site (Figure 4d). This result indicates that the Z-lock switch is reducing activity in the dark state by blocking binding to tubulin. To also test if Z-lock may be reducing αTAT activity by placing strain on the structure we performed the same structure prediction simulations (sampling different linker conformations to dock Zdk against LOV), but with different starting models for αTAT. The αTAT starting models were derived from an elastic network model (elNemo) that predicts conformational changes αTAT is likely to undergo in the folded state[50]. We found that even with the αTAT models that most dramatically perturbed its structure, no changes were observed when simulating Zdk docking with the LOV domain. This indicates that the engineered linkers have enough flexibility to accommodate natural structural perturbations αTAT may undergo, and that the Z-lock switch is not functioning by placing strain on the αTAT structure.

To examine the ability of Z-lock αTAT to acetylate tubulin in living cells, we quantified immunofluorescence staining of acetyl-tubulin in COS7 cells transfected with Z-lock αTAT or controls (Figure 4e). Immunofluorescence images showed increased tubulin acetylation in cells expressing full length αTAT and αTAT core, relative to αTAT dominant negative or untreated cells. Irradiation of Z-lock αTAT induced a two-fold increase in acetylation. (Figure 4f, Supplementary Table 2)

Discussion

In summary, Z-lock provides a versatile means to place a light-controlled, reversible block over important protein sites. Because it is based on steric inhibition, it should be applicable to a wide variety of protein fragments and in some cases complete proteins. We believe the technique will be most useful where a single active site, i.e. a single activity, needs to be controlled and where other regulatory sites are either removed or mutated away. We envision Z-lock will be used to control protein fragments that modulate endogenous targets, like the αTAT fragment used here. Cofilin is an example of an intact protein, but is a special case in that it has essentially one important active site. The modifications that we made to cofilin had little effect on the protein's affinity for actin (Supplementary Fig. 7). As with most optogenetic analogs, upstream regulation was eliminated, so that activity was affected only by irradiation.

The successful completion of the Z-lock analogs here required protein modeling and engineering, primarily to adjust affinities and linkers for intermolecular interactions. There was a trade-off between residual dark state activity and maximal activation. This residual activity is an Achilles heel of most nonchannel optogenetics techniques and often requires careful control of expression level to find conditions where the cell is impacted only upon irradiation. Adjusting Z-dk affinity as exemplified here could tune the balance between 'leakiness' and activity. Expression of a relatively small amount of Z-lock cofilin was sufficient to achieve optogenetic control (Supplementary Fig. 11).

Z-lock cofilin was used to control actin dynamics in vitro and in live cells, and supports a role for cofilin in initiating actin polymerization and in generating invadopodia in tumor

cells[1,2,36]. Precise control of activation kinetics enabled us to show that cofilin activation alone can generate the actin assembly steps produced by EGF stimulation. In the future, we hope to use the technique in live animals to assess cofilin's contribution to tumor cell migration.

Online Methods

Antibodies, DNA Constructs, and Transfection

Antibodies were from the following sources: Cofilin (D3F9) XP® Rabbit mAb (Cell Signaling #5175), β-Actin (8H10D10) Mouse mAb (Cell Signaling #3700), Tks5 (Santa Cruz Biotechnology; sc-30122), Cortactin (Abcam; ab33333). The cDNA of the LOV2 domain from *Avena sativa* (oat) Phototropin1 (L404-L547) was used to generate photo-sensitive constructs. Three variants of LOV2 were used: wild-type, dark state mutant (C450A, L514K, G528A, L531E, and N538E), and lit state mutant (I510E/I539E) (Supplementary Table 2). [24] The cDNA of full-length rat cofilin was used for all constructs. The Z affibodies that selectively bind dark state LOV2 have been described elsewhere. [24] For transient expression in mammalian cells, constructs were cloned into pmCherry-C1 (Clontech Laboratories, Inc.). Cells were transfected with Lipofectamine 2000 (Life Technologies) using the manufacturer's protocol 24 h before imaging. For imaging of living cells, cells were co-transfected with mCherry Z-lock cofilin and a membrane-anchored yPet (KRas C-terminus) to visualize the cell edge. [51]

DNA construction

The cDNA of the LOV2 domain from *Avena Sativa* (oat) Phototropin1 (L404-L547) and the cDNA of cofilin from *Rattus norvegicus* (rat) was used to generate photo-sensitive constructs. All plasmids were generated by Gibson assembly using Gibson Assembly® Master Mix (New England Biolabs, Inc.) according to the manufacturer's protocol. Briefly, fragments were amplified by PCR with Q5® Hot Start High-Fidelity 2X Master Mix (New England Biolabs, Inc.) according to the manufacturer's protocol. Plasmids (specified in Supplementary Table 2) were linearized via restriction digest. Linkers connecting Zdk and LOV2 to cofilin (specified for each construct in Supplementary Table 2) were introduced by including them in the primers used to amplify each fragment for Gibson assembly.

Cell Culture

Rat mammary adenocarcinoma cells (MTLn3) were cultured in MEM-alpha media (Gibco; cat # 12561–056), supplemented with 5% FBS (Gemini Bio-Products; cat # 100106) and antibiotics as described earlier. [52] Cells were maintained in an incubator at 37 C and 5% CO2.

Transiently transfected 293T LINXE cells were used for biochemical assessment of tubulin acetylation levels. Cells were transfected using lipofectamine and plus reagents (Invitrogen). HeLa cells transiently transfected using Fugene6 were plated on plain glass cover slips and used for immunofluorescence imaging.

Protein expression

Proteins were cloned into the bacterial expression vector pET-14b (Novagen) containing an N-terminal His_6-tag. The proteins were expressed in *Escherichia coli* strain BL21(DE3) (New England BioLabs). At OD_{600} = 0.8 – 1.0, cultures were induced with 0.5 mM isopropyl β-D-1-thiogalactopyranoside (IPTG, Sigma). Constructs utilizing lit mutant LOV2 (I510E/I539E) were induced for two hours at 37 C and all other constructs were induced for 5 hours at 37 C. Cultures were pelleted at 5000 RCF and stored at −80 C until purification.

Protein purification

Bacterial pellets were thawed and resuspended in phosphate buffer (20 mM sodium phosphate, 0.5 M NaCl, pH 7.4). A detergent-based protein extraction reagent (10X BugBuster; EMD Millipore) was added to lysate and incubated for 20 minutes at room temperature. Subsequent purification steps were conducted at 4 C. Lysate was cleared via centrifugation at 10,000 RCF and imidazole was added to a final concentration of 40 mM. Proteins were purified via immobilized metal affinity chromatography with a gravity-flow column packed with Ni Sepharose 6 Fast Flow (His GraviTrap; GE Healthcare). The column was equilibrated with phosphate buffer containing 40 mM imidazole. Lysate was applied to the column and the column was washed with phosphate buffer containing 40 mM imidazole. Proteins were eluted with phosphate buffer containing 500 mM imidazole. Purified proteins were concentrated via centrifugal filtration using a regenerated cellulose membrane with a 3 kDa molecular weight cut-off (Amicon® Ultra-4; Millipore Sigma). The buffer was exchanged (10 mM Tris, 50 mM NaCl, pH 7.4) via gel filtration using a spin column packed with a 7 kDa molecular weight cut-off size exclusion resin (Zeba™ Spin Desalting Columns; Fisher Scientific).

Actin Co-sedimentation Assay

This assay was performed using the Actin Binding Protein Spin-Down Assay Biochem Kit (Cytoskeleton, Inc.) according to the manufacturer's protocol with the minor modifications. Briefly, Lyophilized rabbit muscle actin was resuspended to 1 mg/ml in 5 mM Tris-HCL pH 8.0 with 0.2 mM CaCl2. The resuspended solution of rabbit muscle actin was polymerized by adding 10X actin polymerization buffer (500 mM KCL, 20 mM MgCl2, and 10 mM ATP) to a final 1X concentration. Following polymerization the pH of the polymerized actin solution was adjusted to pH 6.8 to limit cofilin-mediated actin depolymerization. After pH adjustment, 30 uL of the polymerized actin solution was added to 20 uL of purified cofilin in storage buffer (10 mM Tris, 50 Mm NaCl, pH 7.4). The reaction mixture contained test protein at a final concentration of 8 μM and F-actin at a final concentration of 12 μM. Reactions were incubated at room temperature for 30 minutes and centrifuged for 1 hour at 164,000 RCF. Supernatant was removed and pellets were resuspended in 50 uL Milli-Q water. Samples were combined with Laemmli sample buffer, boiled for 5 minutes and stored at 4 C. Samples were resolved by SDS-PAGE followed by Western blot using the above mentioned cofilin and β-Actin antibodies. The results were normalized by first measuring the band density of cofilin in the pellet and supernatant fractions. The relative percent of cofilin bound to F-actin was then calculated by dividing the band density of cofilin in the pellet fraction by the sum of the band densities for both the pellet and supernatant fractions.

The average relative percent cofilin bound to F-actin for wild-type cofilin was then used to normalize other measurements.

F-actin severing with Z-lock cofilin

F-actin was polymerized using a mixture of unlabeled-actin (1.4 μM), biotin-actin (0.2 μM) and rhodamine-actin (0.4 μM) in actin polymerization buffer (40 mM pH 7.5 Tris HCl, 10 mM EGTA, 4 mM MgCl2, 100 mM KCl) for 2 hours at room temperature. MatTek glass-bottomed petri dishes were coated with a layer of PEG/PEG-biotin mixture, dried and stored at 4 C before use. Before imaging, the coated dishes were incubated with 0.5 mg/ml streptavidin for 5 minutes, and washed 5X with Tris-HCl. F-actin (0.033 μM) was deposited on the coated dishes for 15 minutes and rinsed 2X with wash buffer (Actin polymerization buffer, 0.5 mg/ml BSA) twice gently. Wash buffer was removed and purified Cofilin or its mutants was added (Z-lock cofilin lit, Z-lock cofilin dark, see Supplementary Table 2). This was diluted in assay solution (10 mM pH 7.5 Tris HCl, 2.5 mM EGTA, 0.25 mM MgCl2, 5 mg/ml BSA, GLOX, 0.5 mM, 10 mM DTT, Protease Inhibitors). Polymerization of F-actin was examined immediately after adding the protein and after indicated times using total internal reflection microscopy (TIRF).

To monitor F-actin severing by Z-lock cofilin with light, we transiently transfected MTLn3 cells with Z-lock cofilin or Z-lock cofilin dark (see Supplementary Table 2). Cell lysate was prepared at 4 C and then loaded onto F-actin coated coverglasses. PA-Cofilin was photoactivated by pulsing blue light (on/off, 1s/1s) (Chroma filter HQ470/40x) for 1 min. The images were taken immediately and after the indicated times.

Western blot quantification

Cofilin and β-Actin band densities were quantified using ImageStudio, with local background subtraction. To calculate F-actin binding, the cofilin band density for the pellet fraction was divided by the sum of the cofilin band intensities for the pellet and supernatant fractions.

Whole-cell photoactivation

Cells were plated on glass-bottom dishes (MatTek Corporation) and allowed to spread overnight protected from light. For F-actin staining cells were plated on acid washed dishes. For invadopodium precursor staining cells were plated on gelatin coated dishes. All work was performed under red light to prevent unintentional photoactivation. Cells were serum-starved 4 hours prior to photoactivation in Leibovitz's L-15 media (Gibco) containing 0.35% BSA. [53] Photoactivation was accomplished with a 470 nm LED array (Mouser Electronics, Inc. part # 828-OVQ12S30B7). The surface of the tissue culture plate was positioned approximately 1 cm away from the LED array, which resulted in a measured power density of 0.064 nW/um2 at 445 nm. During photoactivation, cells were maintained in a cell culture incubator set to 37 C and 5% CO2.

Immunofluorescence

For F-actin and invadopodia analysis MTLn3 cells were fixed with 3.7% paraformaldehyde for 20 min at room temperature and washed 3X with Dulbecco's Phosphate-Buffered Salt

Solution (PBS)(Potassium Chloride 0.2g/L, Potassium Dihydrogen Phosphate 0.2g/L, Sodium Chloride 8g/L, Disodium Phosphate 1.15g/L). Cells were permeabilized with Triton-X-100 0.1% solution in PBS for 5 min and washed 3X with PBS. Cells were blocked with 1% BSA and 1% FBS in PBS for 1 h at room temperature. For invadopodia analysis, cells were stained with primary and secondary antibodies at the manufacturer's suggested dilutions in blocking buffer for 1 hour and washed 3X with PBS after each incubation. For F-actin analysis: DyLight™ 488 Phalloidin (Cell Signaling, 12935) was incubated with cells at 1X concentration for 20 min and washed 3X with PBS.

Preparation of fluorescent gelatin coated dishes

Gelatin was labeled with Alexa-405 dye and glass bottom MatTek dishes were coated with the fluorescent gelatin as described earlier. [54] Briefly, dishes were acid-washed (1N HCl for 10 min) and coated with poly-l-lysine (50 μg/mL for 20 min) followed by Alexa 405-gelatin coating (0.2% gelatin for 10 min). Gelatin matrix was then crosslinked (0.1% glutaraldehyde for 15 min) and inactivated (5 mg/ml $NaBH_4$ for 15 min). After each step dishes were washed (3 × 5 min PBS). Dishes were stored at 4C in 10X Pen-Strep (1,000 IU/mL Penicillin, 1,000μg/mL Streptomycin; ThermoFisher Scientific). All solutions were prepared fresh immediately before use.

Live cell imaging

Cells were plated on acid-washed glass bottom MatTek dishes and allowed to spread overnight, protected from light. Prior to imaging, cells were serum starved in Leibovitz's L-15 media (Gibco) containing 0.35% bovine serum albumin. A closed heated chamber was used during live cell imaging. Imaging was performed using a Zeiss LSM 880 confocal microscope equipped with a Plan-Apochromat 63x oil objective (N.A. 1.40). ZEN software (Zeiss) was used to control the microscope and acquire images at each time point. A GaAsP detector with tunable emission collection windows (Zeiss) was used for detection. YFP images were acquired using a 514 nm Argon laser (25% power) with a collection window of 525 – 580 nm. mCherry images were acquired using a 561 nm DPSS laser (20% laser power) with a collection window of 580 – 650 nm. LOV2 photoactivation was accomplished with a 488 nm Argon laser (1% power) that irradiated a preselected region every 10 seconds. Images were acquired every 2.5 seconds.

Directionality Analysis

Changes in cell directionality were quantified using the directionality index, which is defined as the cosine of the angle between the site of photoactivation and the vector direction of cell movement. [10] The vector direction of cell movement was determined by measuring the cell centroid at two different time points. We used Fiji/Imagej to define the cell centroids, following thresholding of each cell. Fiji/Image calculates the centroid by taking the average of the x and y coordinates of all of the pixels for the thresholded cell. The site of photoactivation was determined by measuring the centroid of the photoactivation ROI using Fiji/ImageJ. The directionality index was assessed for two intervals. First, two minutes prior to photoactivation until the time of photoactivation, which measured cell movement before photoactivation. Second, from the time of photoactivation until two minutes after, which assessed potential changes in directionality in response to photoactivation.

Measurement of F-actin content

Cells fixed and stained with phalloidin were imaged on an Olympus IX-81 microscope equipped with a UPlanFLN 40x objective (Pil, N.A 1.30). Metamorph software (Molecular Devices) was used to control the microscope and acquire images. Dylight 488 and mCherry images were acquired using a 100 Watt mercury arc lamp with a 1% ND filter and a 500–550 nm or 565–595 nm band-pass filter respectively, with 1 second exposure for each channel. Flat field correction was applied to each image using a custom MatLab script. [55] Corrected images were thresholded with Otsu's method[56] using Fiji/ImageJ to generate masks for individual cells. For each image, a region without cells was used to determine background intensity for background subtraction. Mean phalloidin intensity (shade corrected and background subtracted) was measured for individual cells using previously generated masks. Experimental replicates were imaged on the same day to enable comparison based on signal intensity. Cell intensities for each condition were averaged for the sake of comparison.

Invadopodium Precursor Analysis

MTLn3 cells transfected with light-insensitive control or mCherry Z-lock cofilin were irradiated for 1 min and fixed at 1, 3, 5- and 30-min post photoactivation. Cells were stained with anti-Cortactin and antiTks5 antibodies and imaged on a Delta Vision epi- fluorescence microscope (Applied Precision Inc.), equipped with a CoolSNAP HQ2 camera and a 60x, NA 1.42 objective lens. Invadopodium precursors were identified as Tks5- and cortactin-positive puncta. The number of invadopodium precursors per cell were quantified in Fiji/ImageJ.

Modeling of linkers connecting Zdk and LOV2 to cofilin

Structural models were generated using the RosettaRemodel package with the Rosetta3.5 series software. [31,48] This package was designed to provide a framework for flexible protein design utilizing the loop modeling tools in Rosetta. In this case, we used the domain insertion protocol to model the orientation of the Zdk-LOV complex relative to cofilin with Zdk and LOV attached to the N- and C-terminus of cofilin (PDB 4BEX), respectively. [57] For both Zdk1 (PDB 5EFW) and Zdk2 (PDB 5DJT), we modeled linkers of different length and composition and assessed whether the Zdk-LOV complex reliably orientated over the actin binding interface of cofilin. [24]

Computational identification of Zdk2 point mutants

The change in binding energy for Zdk2 point mutants was calculated using the ddG monomer package with the Rosetta3.5 series of software. [32]The package was designed to predict the change in stability (the ddG) of a protein induced by a point mutation. In this case, we calculated the ddG induced by several point mutants for both Zdk2 and the Zdk2-LOV complex, using the PDB structure 5DJT as a starting point. Subtracting the ddG for Zdk2 from the ddG for the Zdk2-LOV complex yielded the change in binding energy. The shift in binding curve was calculated using the following equation:

$$\Delta\Delta G = -RTln\frac{K_{d2}}{K_{d1}}$$

where ΔΔG is the change in binding energy, R is the gas constant, T is the temperature, and K_{d2} / K_{d1} is the shift in the binding curve.

Statistical analysis

Statistical significance was determined by either *t*-test (normally distributed dataset) or Mann–Whitney test (non-normally distributed dataset). Normality of each dataset was tested with D'Agostino & Pearson normality test. For selected datasets, we used a Tukey box-and-whisker plot. The ends of the box denote the interquartile range (IQR) and the median is marked as a line across the box. Whiskers represent either the largest data point less than or equal to 1.5 times the IQR (upper whisker) or the smallest data point more than or equal to −1.5 times the IQR (lower whisker). Outliers (any value larger than 1.5 times the IQR or smaller than −1.5 times the IQR) are displayed as dots. All statistical analysis was conducted with GraphPad Prism 7. During optimization of linkers and Zdk2 mutants, some constructs were tested only once (Figure 2a and 2g). The final design used for cell-based experiments was retested by actin co-sedimentation assay in three independent experiments and the data is shown in Figure 2c. Microscopy images are representative of three independent experiments.

Biochemical validation of Z-lock αTAT

A 5sec on- 5sec off regime of blue light exposure was achieved using an LED-panel constructed for placement in a 37 °C, 5% CO_2 incubator and controlled with an Arduino board. The blue light intensity on the cells was approx. 0.05 nW/μm^2. Cells were kept under blue light for 30 minutes and then lysed in lysis buffer on ice for 20min. Lysates were loaded on SDS-PAGE gels and transferred to PVDF membranes for Western blotting. The samples were stained with monoclonal anti-AcetylTubulin antibody (Sigma: 6–11B-1,) for acetylated alpha tubulin and anti-FLAG antibody (Abcam: ab49763) for either αTAT or Z-lock αTAT at 4 C overnight. The samples were then wash and stained with dye-labeled secondary antibodies (ThermoFisher: Dylight 800; Bio-rad: Starbright 700) at room temperature for 1 hour.

Immunofluorescence of microtubule acetylation

Cells were fixed with ice-cold 100% methanol for 3 minutes before permeabilizing with 0.5% Triton-X100. Staining was performed with the same primary antibodies as above and with a pair of dye-conjugated secondary antibodies (Abcam: ab150105, ab175471). All immunofluorescence buffers were made from a 10x stock of BRB80 with 0.1% Triton-X100. Stained cells were mounted in prolong gold (ThermoFish Scientific) and imaged on an Olympus spinning disk confocal microscope with a 60x objective. Intensity measurements were made by masking the cells in Fiji/ImageJ and normalizing acetylation intensity to expression level.

Data and Code Availability Statement

The data that support the findings of this study are available from the corresponding authors upon request. Code is available from the authors upon request or at hahnlab.com.

Supplementary Material

Refer to Web version on PubMed Central for supplementary material.

Acknowledgments

We thank the NIH for supporting this work (GM122596 to K.M.H., CA150344 and CA216248 to J.S.C.). O.J.S. is a recipient of a Ruth L. Kirschstein National Research Service Award (1F31CA192739). We thank M. Azoitei for assisting with Rosetta modeling, T. Watanabe for assistance with localized photoactivation experiments, and Chelsea Onyeji for help with cloning and biochemical assays.

References

1. Bravo-Cordero JJ, Magalhaes MAO, Eddy RJ, Hodgson L & Condeelis J Functions of cofilin in cell locomotion and invasion. Nat. Rev. Mol. Cell Biol 14, 405–415 (2013). [PubMed: 23778968]
2. Sidani M et al. Cofilin determines the migration behavior and turning frequency of metastatic cancer cells. J. Cell Biol 179, 777–791 (2007). [PubMed: 18025308]
3. Zoncu R et al. Loss of endocytic clathrin-coated pits upon acute depletion of phosphatidylinositol 4,5-bisphosphate. Proc. Natl. Acad. Sci. USA 104, 3793–3798 (2007). [PubMed: 17360432]
4. Oser M & Condeelis J The cofilin activity cycle in lamellipodia and invadopodia. J. Cell Biochem 108, 1252–1262 (2009). [PubMed: 19862699]
5. DesMarais V, Ghosh M, Eddy R & Condeelis J Cofilin takes the lead. J. Cell Sci 118, 19–26 (2005). [PubMed: 15615780]
6. Chen Q & Pollard TD Actin filament severing by cofilin dismantles actin patches and produces mother filaments for new patches. Curr. Biol 23, 1154–1162 (2013). [PubMed: 23727096]
7. Yang N et al. Cofilin phosphorylation by LIM-kinase 1 and its role in Rac-mediated actin reorganization. Nature 393, 809–812 (1998). [PubMed: 9655398]
8. Aizawa H, Sutoh K & Yahara I Overexpression of cofilin stimulates bundling of actin filaments, membrane ruffling, and cell movement in Dictyostelium. J. Cell Biol 132, 335–344 (1996). [PubMed: 8636212]
9. Aizawa H et al. Phosphorylation of cofilin by LIM-kinase is necessary for semaphorin 3A-induced growth cone collapse. Nat. Neurosci 4, 367–373 (2001). [PubMed: 11276226]
10. Ghosh M et al. Cofilin promotes actin polymerization and defines the direction of cell motility. Science 304, 743–746 (2004). [PubMed: 15118165]
11. Riedl J et al. Lifeact: a versatile marker to visualize F-actin. Nat. Methods 5, 605–607 (2008). [PubMed: 18536722]
12. Hughes RM & Lawrence DS Optogenetic engineering: light-directed cell motility. Angew. Chem. Int. Ed. Engl 53, 10904–10907 (2014). [PubMed: 25156888]
13. Courtemanche N, Pollard TD & Chen Q Avoiding artefacts when counting polymerized actin in live cells with LifeAct fused to fluorescent proteins. Nat. Cell Biol 18, 676–683 (2016). [PubMed: 27159499]
14. Dagliyan O et al. Engineering extrinsic disorder to control protein activity in living cells. Science 354, 1441–1444 (2016). [PubMed: 27980211]
15. Wu YI et al. A genetically encoded photoactivatable Rac controls the motility of living cells. Nature 461, 104–108 (2009). [PubMed: 19693014]
16. Hayashi-Takagi A et al. Labelling and optical erasure of synaptic memory traces in the motor cortex. Nature 525, 333–338 (2015). [PubMed: 26352471]
17. Strickland D et al. TULIPs: tunable, light-controlled interacting protein tags for cell biology. Nat. Methods 9, 379–384 (2012). [PubMed: 22388287]
18. Strickland D, Moffat K & Sosnick TR Light-activated DNA binding in a designed allosteric protein. Proc. Natl. Acad. Sci. USA 105, 10709–10714 (2008). [PubMed: 18667691]

19. Yi JJ, Wang H, Vilela M, Danuser G & Hahn KM Manipulation of endogenous kinase activity in living cells using photoswitchable inhibitory peptides. ACS Synth. Biol 3, 788–795 (2014). [PubMed: 24905630]
20. Weitzman M & Hahn KM Optogenetic approaches to cell migration and beyond. Curr. Opin. Cell Biol. 30, 112–120 (2014). [PubMed: 25216352]
21. Wang X, Chen X & Yang Y Spatiotemporal control of gene expression by a light-switchable transgene system. Nat. Methods 9, 266–269 (2012). [PubMed: 22327833]
22. Zoltowski BD, Vaccaro B & Crane BR Mechanism-based tuning of a LOV domain photoreceptor. Nat. Chem. Biol 5, 827–834 (2009). [PubMed: 19718042]
23. Kawano F, Aono Y, Suzuki H & Sato M Fluorescence imaging-based high-throughput screening of fast- and slow-cycling LOV proteins. PLoS One 8, e82693 (2013). [PubMed: 24367542]
24. Wang H et al. LOVTRAP: an optogenetic system for photoinduced protein dissociation. Nat. Methods 13, 755–758 (2016). [PubMed: 27427858]
25. Wang H & Hahn KM LOVTRAP: A Versatile Method to Control Protein Function with Light. Curr. Protoc. Cell Biol 73, 21.10.1–21.10.14 (2016). [PubMed: 27906450]
26. Yu Y & Lutz S Circular permutation: a different way to engineer enzyme structure and function. Trends Biotechnol. 29, 18–25 (2011). [PubMed: 21087800]
27. Zhou XX, Chung HK, Lam AJ & Lin MZ Optical control of protein activity by fluorescent protein domains. Science 338, 810–814 (2012). [PubMed: 23139335]
28. Zhou XX, Fan LZ, Li P, Shen K & Lin MZ Optical control of cell signaling by single-chain photoswitchable kinases. Science 355, 836–842 (2017). [PubMed: 28232577]
29. Lai FPL et al. Arp2/3 complex interactions and actin network turnover in lamellipodia. EMBO J. 27, 982–992 (2008). [PubMed: 18309290]
30. Pope B & Weeds AG Binding of pig plasma gelsolin to F-actin and partial fractionation into calcium-dependent and calcium-independent forms. Eur. J. Biochem. 161, 85–93 (1986). [PubMed: 3023089]
31. Huang P-S et al. RosettaRemodel: a generalized framework for flexible backbone protein design. PLoS One 6, e24109 (2011). [PubMed: 21909381]
32. Kellogg EH, Leaver-Fay A & Baker D Role of conformational sampling in computing mutation-induced changes in protein structure and stability. Proteins 79, 830–838 (2011). [PubMed: 21287615]
33. Chan AY, Bailly M, Zebda N, Segall JE & Condeelis JS Role of cofilin in epidermal growth factor-stimulated actin polymerization and lamellipod protrusion. J. Cell Biol 148, 531–542 (2000). [PubMed: 10662778]
34. Development and Biologic Properties of Malignant Cell Sublines and Clones of a Spontaneously Metastasizing Rat Mammary Adenocarcinoma23. JNCI: Journal of the National Cancer Institute (1982). doi:10.1093/jnci/68.3.507
35. Chan AY et al. EGF stimulates an increase in actin nucleation and filament number at the leading edge of the lamellipod in mammary adenocarcinoma cells. J. Cell Sci 111 (Pt 2), 199–211 (1998). [PubMed: 9405304]
36. Eddy RJ, Weidmann MD, Sharma VP & Condeelis JS Tumor Cell Invadopodia: Invasive Protrusions that Orchestrate Metastasis. Trends Cell Biol. 27, 595–607 (2017). [PubMed: 28412099]
37. Yamaguchi H et al. Molecular mechanisms of invadopodium formation: the role of the N-WASP-Arp2/3 complex pathway and cofilin. J. Cell Biol 168, 441–452 (2005). [PubMed: 15684033]
38. Oser M et al. Cortactin regulates cofilin and N-WASp activities to control the stages of invadopodium assembly and maturation. J. Cell Biol 186, 571–587 (2009). [PubMed: 19704022]
39. Beaty BT et al. β1 integrin regulates Arg to promote invadopodial maturation and matrix degradation. Mol. Biol. Cell 24, 1661–75, S1 (2013). [PubMed: 23552693]
40. Haggarty SJ, Koeller KM, Wong JC, Grozinger CM & Schreiber SL Domain-selective small-molecule inhibitor of histone deacetylase 6 (HDAC6)-mediated tubulin deacetylation. Proc. Natl. Acad. Sci. USA 100, 4389–4394 (2003). [PubMed: 12677000]

41. Hubbert C et al. HDAC6 is a microtubule-associated deacetylase. Nature 417, 455–458 (2002). [PubMed: 12024216]
42. North BJ, Marshall BL, Borra MT, Denu JM & Verdin E The human Sir2 ortholog, SIRT2, is an NAD+-dependent tubulin deacetylase. Mol. Cell 11, 437–444 (2003). [PubMed: 12620231]
43. Miotto B & Struhl K HBO1 histone acetylase activity is essential for DNA replication licensing and inhibited by Geminin. Mol. Cell 37, 57–66 (2010). [PubMed: 20129055]
44. Borra MT, Langer MR, Slama JT & Denu JM Substrate specificity and kinetic mechanism of the Sir2 family of NAD+-dependent histone/protein deacetylases. Biochemistry 43, 9877–9887 (2004). [PubMed: 15274642]
45. Shida T, Cueva JG, Xu Z, Goodman MB & Nachury MV The major alpha-tubulin K40 acetyltransferase alphaTAT1 promotes rapid ciliogenesis and efficient mechanosensation. Proc. Natl. Acad. Sci. USA 107, 21517–21522 (2010). [PubMed: 21068373]
46. Friedmann DR, Aguilar A, Fan J, Nachury MV & Marmorstein R Structure of the α-tubulin acetyltransferase, αTAT1, and implications for tubulin-specific acetylation. Proc. Natl. Acad. Sci. USA 109, 19655–19660 (2012). [PubMed: 23071314]
47. Szyk A et al. Molecular basis for age-dependent microtubule acetylation by tubulin acetyltransferase. Cell 157, 1405–1415 (2014). [PubMed: 24906155]
48. Leaver-Fay A et al. ROSETTA3: an object-oriented software suite for the simulation and design of macromolecules. Meth. Enzymol 487, 545–574 (2011). [PubMed: 21187238]
49. Kuhlman B, Jacobs T & Linskey T Computational design of protein linkers. Methods Mol. Biol 1414, 341–351 (2016). [PubMed: 27094301]
50. Suhre K & Sanejouand Y-H ElNemo: a normal mode web server for protein movement analysis and the generation of templates for molecular replacement. Nucleic Acids Res. 32, W610–4 (2004). [PubMed: 15215461]

References

51. Li T et al. Incorporation of DDR2 clusters into collagen matrix via integrin-dependent posterior remnant tethering. Int. J. Biol. Sci 14, 654–666 (2018). [PubMed: 29904280]
52. Sharma VP et al. Tks5 and SHIP2 regulate invadopodium maturation, but not initiation, in breast carcinoma cells. Curr. Biol 23, 2079–2089 (2013). [PubMed: 24206842]
53. Leibovitz A The growth and maintenance of tissue–cell cultures in free gas exchange with the atmosphere1. Am. J. Epidemiol 78, 173–180 (1963).
54. Sharma VP, Entenberg D & Condeelis J High-resolution live-cell imaging and time-lapse microscopy of invadopodium dynamics and tracking analysis. Methods Mol. Biol 1046, 343–357 (2013). [PubMed: 23868599]
55. Hodgson L, Shen F & Hahn K Biosensors for characterizing the dynamics of rho family GTPases in living cells. Curr. Protoc. Cell Biol Chapter 14, Unit 14.11.1–26 (2010). [PubMed: 20521232]
56. Otsu N A Threshold Selection Method from Gray-Level Histograms. IEEE Trans. Syst. Man. Cybern 9, 62–66 (1979).
57. Klejnot M et al. Analysis of the human cofilin 1 structure reveals conformational changes required for actin binding. Acta Crystallogr. Sect. D, Biol. Crystallogr 69, 1780–1788 (2013). [PubMed: 23999301]

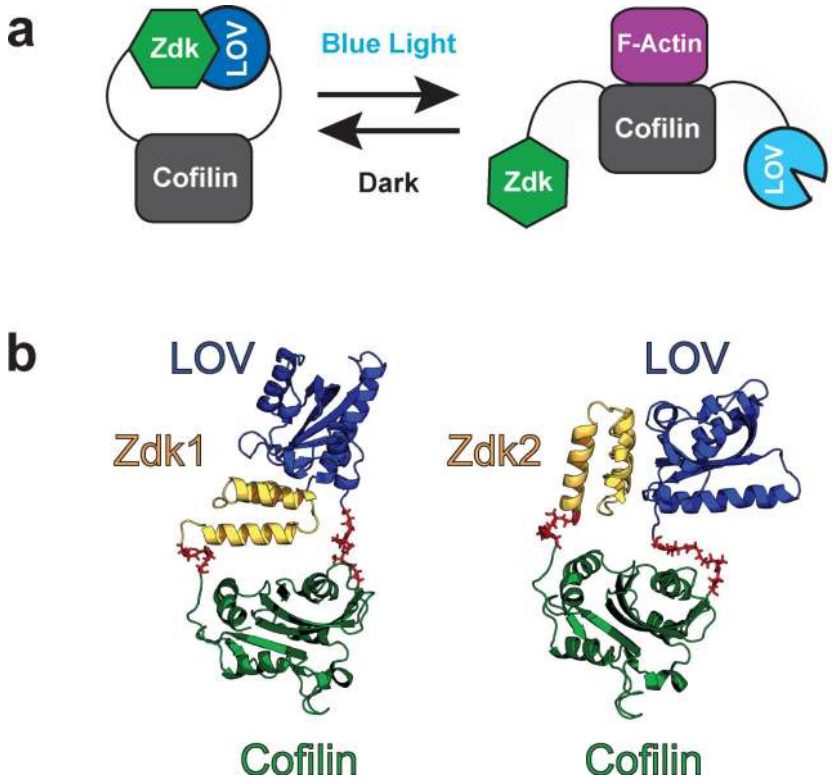

Figure 1. Design of Z-lock cofilin.

a. Design of Z-lock cofilin.Cofilin (gray) is fused at its N-terminus to Zdk (green) and at its C-terminus to LOV (blue). In the dark, Zdk binding to LOV blocks cofilin binding to F-actin (purple).

b. Rosetta-based structure prediction for designs incorporating Zdk1 versus Zdk2. Linker residues connecting Zdk and LOV to cofilin are shown in red.

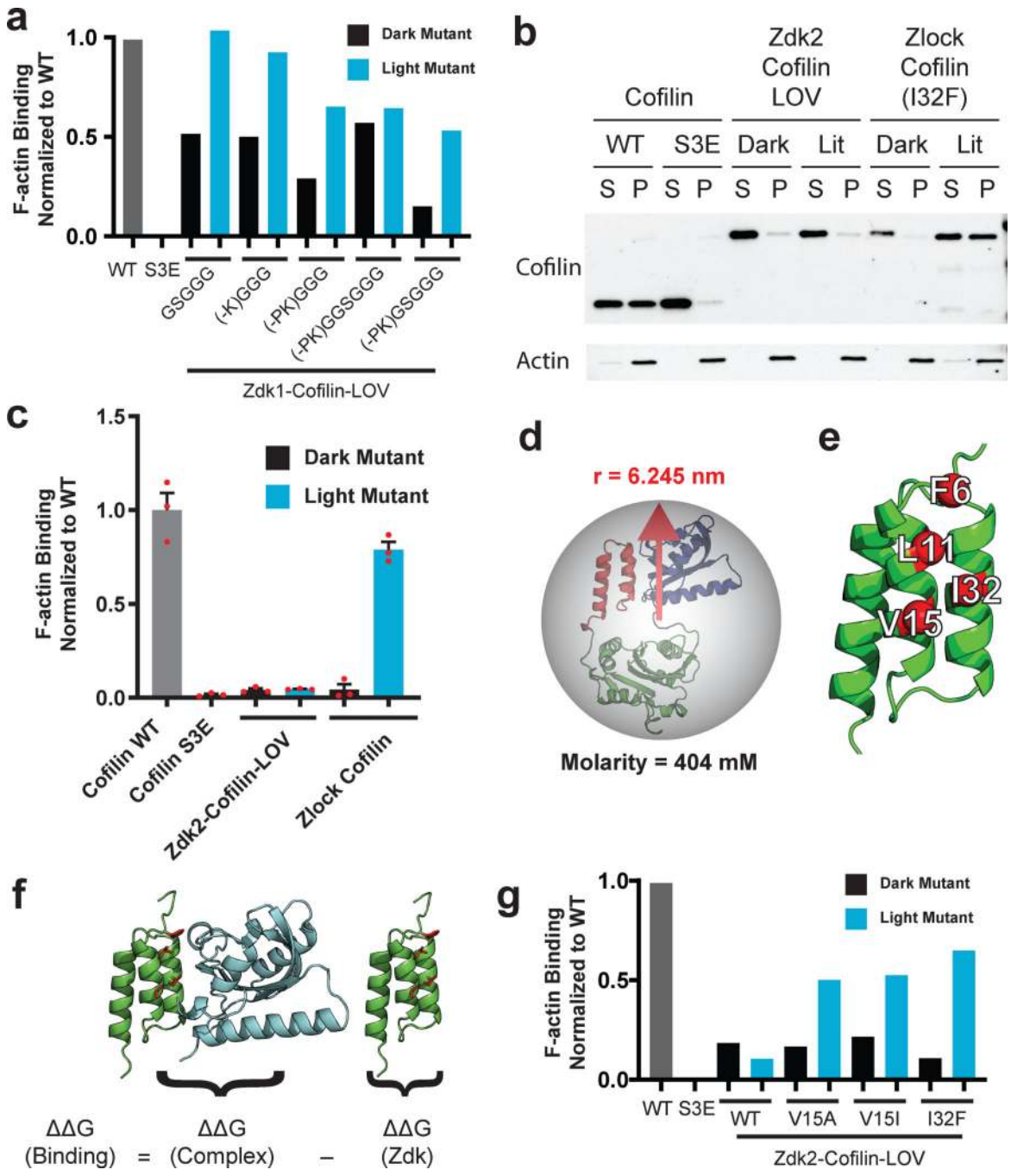

Figure 2. Optimization of designs based on Zdk1 and Zdk2.

a. Actin co-sedimentation assay to measure binding of cofilin to F-actin. Wild type and S3E inactive cofilin mutants are shown as controls. Different linkers connecting Zdk1 to cofilin are shown on the x-axis. Parentheses indicate residues truncated from the Zdk1 C-terminus. Dark and lit state mutants were used to assess light-dependent changes in cofilin F-actin binding (Supplementary Table 2). In this initial screening study, each variant was tested once.

b. c.) Actin co-sedimentation assay to measure binding of cofilin to F-actin. Wild-type cofilin and S3E constitutively inactive cofilin mutants are shown as controls. Light-dependent binding to F-actin was tested using LOV2 mutants that mimic the dark state and lit state (Supplementary Table 2). The center and error bars in **c** represent mean ± SEM from three independent experiments. (See full gels in Supplementary Fig. 5)

d. Estimation of LOV2 effective molarity. The volume of a sphere enclosing the Zdk2-based design was determined and used to estimate the effective LOV2 molarity encountered by Zdk2.

e. Four residues (shown in red) along the first and second helices of Zdk2 were mutated to generate a reduced affinity variant of Zdk2.

f. The change in Gibbs free energy (ΔΔG) for Zdk2 mutants was calculated for the Zdk2-LOV2 complex (ΔΔG complex) and Zdk2 in isolation (ΔΔG Zdk2). Subtracting the two values yielded the change in binding energy of the complex (ΔΔG binding).

g. Actin co-sedimentation assay to measure the binding of cofilin to F-actin. Wild type and S3E inactive cofilin mutant are shown as controls. Zdk2 mutants are shown on the x-axis. Dark and lit state mutants (Supplementary Table 2) were used to assess light-dependent changes in cofilin F-actin binding. In this initial screen, each variant was tested only once.

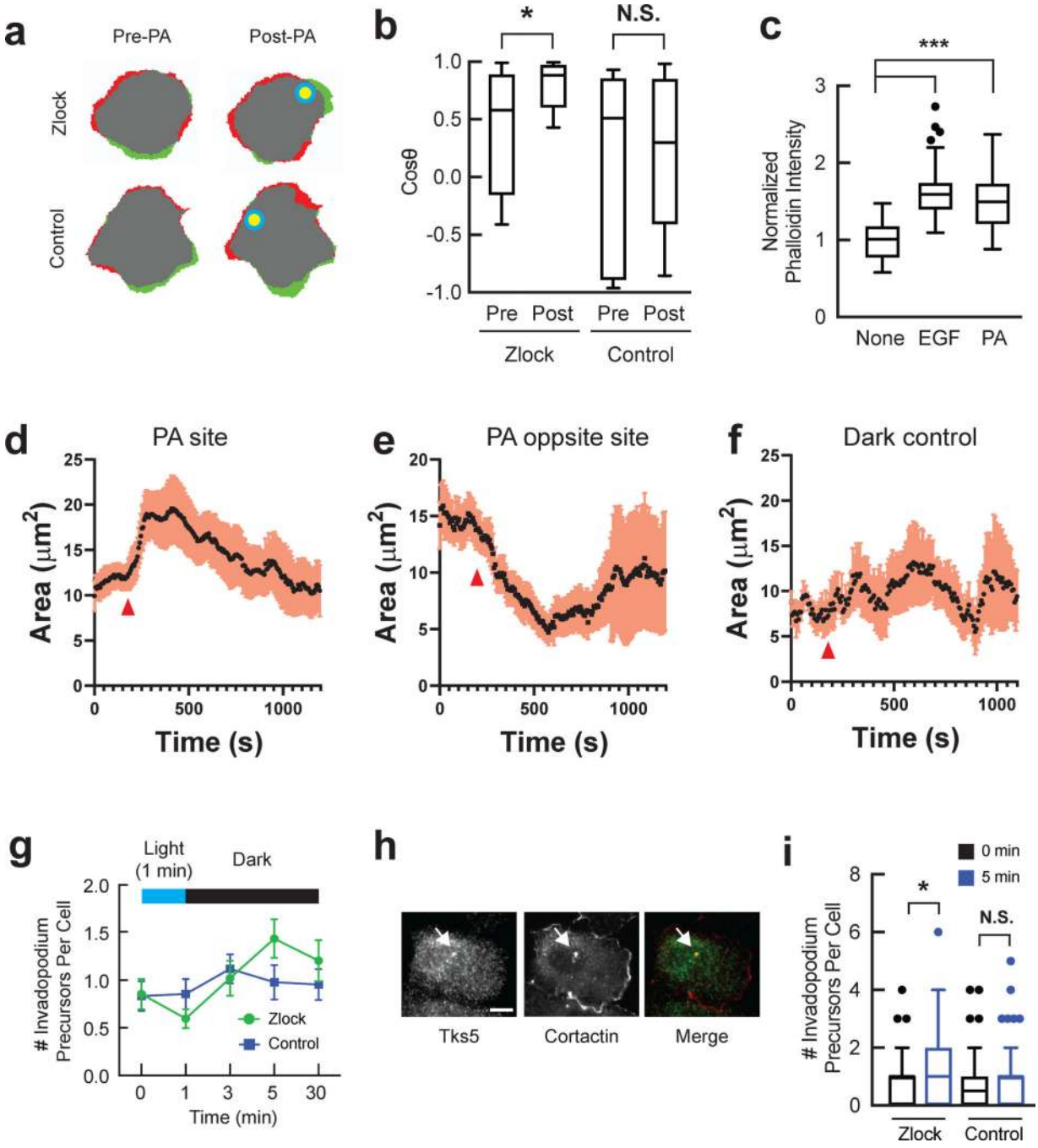

Figure 3. Effect of Z-lock cofilin activation on leading edge protrusions and invadopodium formation in tumor cells.

a. Cell perimeter before (left) and after (right) photoactivation. Retraction = red; protrusion = green; no change = grey. The site of photoactivation is indicated by the yellow circle. The dark state mutant of Z-lock cofilin is shown as a control. (Z-lock: n= 8 cells; Control: n= 9 cells) (Three independent experiments)

b. Analysis of directional migration in response to irradiation of either Z-lock cofilin or Z-lock cofilin dark state mutant (Supplementary Table 2). The cosine of the angle between the

site of photoactivation and the vector of cell movement were calculated for two minutes before (Pre-PA) and after photoactivation (Post-PA). Photoactivation led to an increase in the cosine value for Z-lock cofilin (p-value = 0.0271; $n = 8$ cells, paired two-tailed t-test) but not for the Z-lock cofilin dark state mutant (p-value = 0.5782; $n = 9$ cells, paired two-tailed t-test). Cosine value for Pre-PA Z-lock cofilin and Z-lock cofilin dark state mutant were not significantly different (p-value = 0.3523, unpaired two-tailed t-test). Tukey box-and-whisker plot shown with outliers displayed as dots. (Three independent experiments)

c. F-actin content of MTLn3 cells expressing Z-lock cofilin that were either unstimulated ($n = 34$ cells), stimulated with 5 nM EGF ($n = 56$ cells), or photoactivated (PA) ($n = 51$ cells). F-actin content was assessed following fixation and phalloidin staining. PA cells were irradiated for one minute and fixed three minutes after photoactivation. Phalloidin intensity was significantly different for both EGF ($p < 0.0001$) and PA ($p < 0.0001$) relative to unstimulated cells. EGF and PA phalloidin intensity were not significantly different from one another ($p = 0.0521$). P-value was calculated using Mann–Whitney test, two-sided. Tukey box-and-whisker plot shown with outliers displayed as dots. (Three independent experiments)

d. e. f.) d Cell area change within the PA spot. Red arrow indicates the start of photoactivation. Cells were irradiated for 60 s using a 500 ms pulse of blue light every second (n=9). **e** A spot opposite the site of PA is monitored (n=9). **f** Cell area change within the PA spot for cells expressing the dark mutant of Z-lock cofilin (n=9) (Supplementary Table 2). Data is shown as mean ± SEM. (Three independent experiments)

g. Effect of photoactivation on the number of invadopodium precursors in MTLn3 cells expressing Z-lock cofilin versus a dark state mutant. Data is shown as mean ± SEM. Z-lock cofilin (0 min: $n = 41$ cells; 1 min: $n = 57$ cells; 3 min: $n = 51$ cells; 5 min: $n = 46$ cells; 30 min: $n = 54$). Control (0 min: $n = 48$; 1 min: $n = 48$; 3 min: $n = 51$; 5 min: $n = 45$; 30 min: $n = 43$). (Three independent experiments)

h. Representative immunofluorescence images of MTLn3 cell stained for Tks5 and cortactin to identify invadopodium precursors (indicated by the white arrow). Scale bar: 10 μm.

i. Change in number of invadopodium precursors per cell following photoactivation, based on the data in **Figure 3g**. Photoactivation resulted in a significant increase of invadopodium precursors for Z-lock cofilin ($p = 0.0332$, Mann–Whitney test, two-sided) but not for the Z-lock cofilin dark state mutant ($p = 0.6001$, Mann–Whitney test, two-sided) at 5 min post-photoactivation. Tukey box-and-whisker plot shown with outliers displayed as dots.

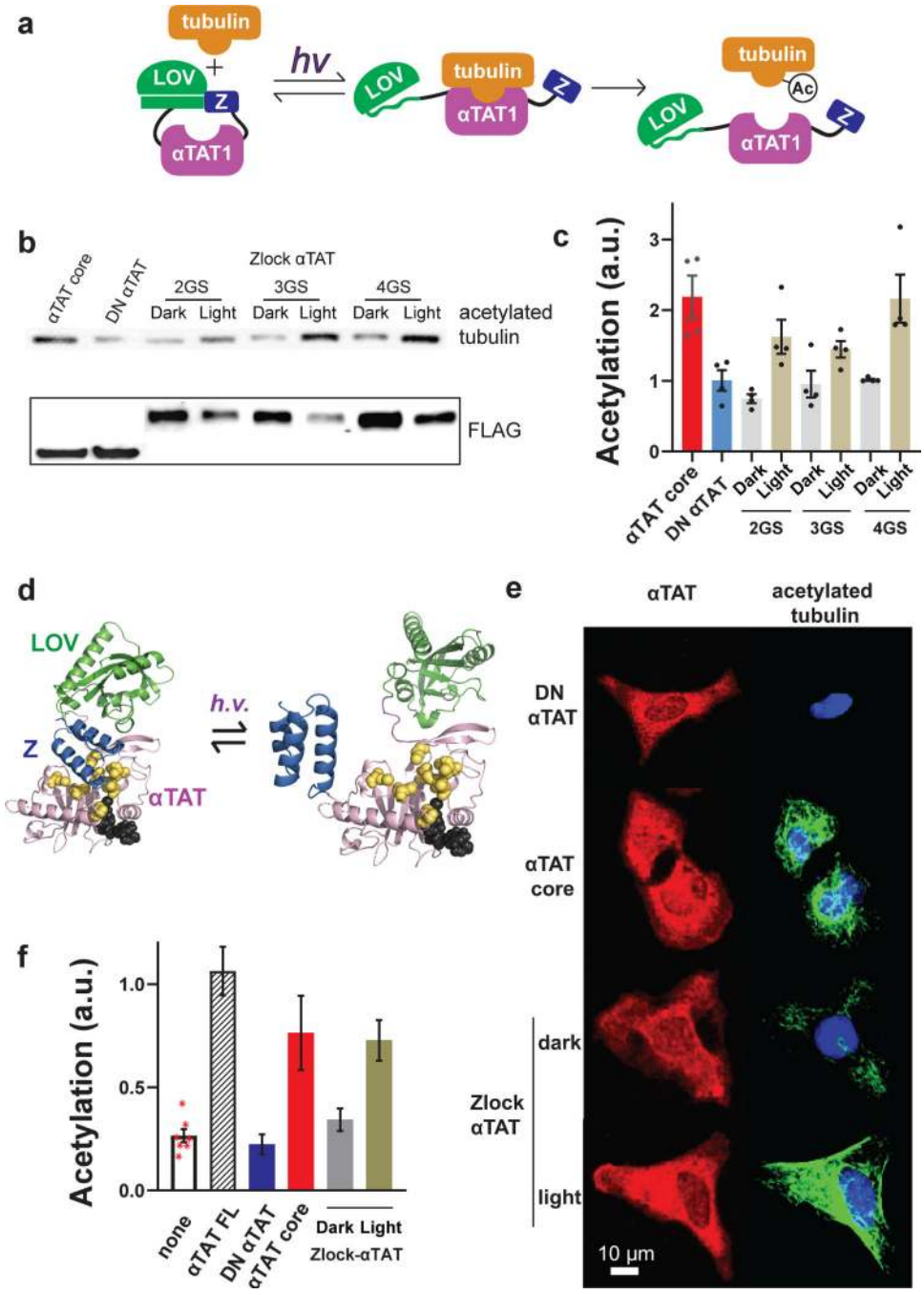

Figure 4. Z-lock αTAT

a. Design of Z-lock αTAT showing light-induced acetylation of tubulin.

b. c.) b Western blotting shows microtubule acetylation in 293TLinXE cells resulting from three versions of LOV-αTAT-Zdk (2GS/3GS/4GS) in the dark vs light (Supplementary Table 2). The enzyme core (a.a. 2–237) was used as a positive control (αTAT core) and a core mutant with reduced activity (Q58A/D157N) was used as a negative control (DN αTAT). **c** Quantification of Western blotting in **b** showed how linker modification affected the activity in the light versus the dark. Acetylation levels were normalized to construct expression (see

FLAG blotting in **b**). The 3GS linker version was denoted Z-lock αTAT. Data is shown as mean ± SEM (n=4). (See full gels in Supplementary Fig. 13) (Three independent experiments)

d. Rosetta-based prediction of Z-lock αTAT structures in the dark and lit states.

e. f.) e Immunofluorescence images showing the light-mediated acetylation of microtubules in HeLa cells expressing indicated constructs. Cells expressing Z-lock αTAT were examined with and without blue light activation. **f** Quantification of acetylation level from immunofluorescence data. Values are normalized for construct expression level. Data is shown as mean ± SEM (none: n = 7; αTAT FL: n = 11; DN αTAT: n = 34; αTAT core: n = 44; Z-lock Dark: n = 43; Z-lock Light: n = 57). (Three independent experiments)